International Journal of Minerals, Metallurgy and Materials
Volume 29, Number 2, February 2022, Page 305
https://doi.org/10.1007/s12613-020-2201-2

Effect of graphene oxide on the corrosion, mechanical and biological properties of Mg-based nanocomposite

*Saeid Jabbarzare*1), *Hamid Reza Bakhsheshi-Rad*2),✉, *Amir Abbas Nourbakhsh*1),✉, *Tahmineh Ahmadi*1), *and Filippo Berto*3)

1) Department of Materials Science, Shahreza Branch, Islamic Azad University, Shahreza, Iran

2) Advanced Materials Research Center, Department of Materials Engineering, Najafabad Branch, Islamic Azad University, Najafabad, Iran

3) Department of Mechanical and Industrial Engineering, Norwegian University of Science and Technology, 7491 Trondheim, Norway

(Received: 3 July 2020; revised: 14 September 2020; accepted: 21 September 2020)

Abstract: This study investigates the effect of graphene oxide (GO) on the mechanical and corrosion behavior, antibacterial performance, and cell response of Mg–Zn–Mn (MZM) nanocomposite. MZM/GO nanocomposites with different amounts of GO (i.e., 0.5wt%, 1.0wt%, and 1.5wt%) were fabricated by the semi-powder metallurgy method. The influence of GO on the MZM nanocomposite was analyzed through the hardness, compressive, corrosion, antibacterial, and cytotoxicity tests. The experimental results showed that, with the increase in the amount of GO (0.5wt% and 1.5wt%), the hardness value, compressive strength, and antibacterial performance of the MZM nanocomposite increased, whereas the cell viability and osteogenesis level decreased after the addition of 1.5wt% GO. Moreover, the electrochemical examination results showed that the corrosion behavior of the MZM alloy was significantly enhanced after encapsulation in 0.5wt% GO. In summary, MZM nanocomposites reinforced with GO can be used for implant applications because of their antibacterial performance and mechanical property.

Keywords: magnesium-based nanocomposite; graphene oxide; powder metallurgy method; mechanical property; antibacterial activity; biocompatibility

1. Introduction

Currently, because magnesium (Mg) alloys have more benefits than common metallic materials, ceramics, and biodegradable polymers, their biomedical applications have been increasing. In terms of mechanical features, metals have higher mechanical strength and fracture toughness than ceramics or polymers; thus, metals are more appropriate for load-bearing usages than ceramics or polymers [1–2]. The density of human cortical bone (1.75 g/cm^3) is similar to the density of Mg (1.738 g/cm^3) and Mg alloys (1.75–1.85 g/cm^3) but lower than the density of biomedical titanium alloy Ti6Al4V (4.47 g/cm^3) [3–4]. In terms of biocompatibility, certain amounts of Mg ions in the human body are connected with many metabolic reactions and biological mechanisms [5–6]. Mg alloys are suitable orthopedic and cardiovascular implants because further surgery to remove them is not needed [7–8]. However, an important drawback of Mg-based implants is that they do not have good resistance against corrosion in physiological environments [9]. Mechanical strength could be significantly reduced by rapid and uncontrollable corrosion processes, which leads to premature failure [10]. Moreover, the health of patients who have such implants could be at risk because of the evolution of hydrogen gas and alkalinization of the environments close to the interface between implant and tissue [11]. Therefore, to achieve the secure deployment of biomedical devices, the degradation/corrosion rate of Mg alloys needs to be controlled [12]. In this context, several methods, such as alloying, powder metallurgy (PM), and surface modification strategies, have been used in an extensive number of studies that aimed to solve the problem of corrosion in Mg alloys [13–14]. Among the best methods to enhance the corrosion resistance of porous Mg are PM processes, such as mechanical alloying [15–17].

Furthermore, the PM method is suitable for synthesizing Mg-based bioceramic composite because bioceramics and nonequilibrium phases can be added to the Mg-based matrix. However, variances between Mg and bioceramics are observed and atmospheric control is needed in the casting method [12]. In this study, to meet the clinical requirements, zinc (Zn) and manganese (Mn) were added to enhance mechanical strength and corrosion resistance [18]. Zn and Mn are present in all body tissues and are among the most common nutritional elements [7]. Mechanical strength and corrosion resistance are commonly increased in Mg alloys by adding

---

✉ Corresponding authors: Hamid Reza Bakhsheshi-Rad E-mail: rezabakhsheshi@gmail.com, rezabakhsheshi@pmt.iaun.ac.ir;
Amir Abbas Nourbakhsh E-mail: anourbakhs@yahoo.com

Zn and Mn with the solubility rate of 6.2wt% [19]. However, the application of Mg-based nanocomposites causes some post-surgery problems and has been limited because of their inadequate antibacterial features [6]. Currently, the prevention of bacterial colonization and infection propagation is vital to human health. Because antibacterial agents have high efficiency and a long lifetime without any significant side effect, they are applied in sterilizing facilities to sustain the bulk features of materials and decrease the cost [20–21]. The addition of an antibacterial agent is the appropriate method for killing bacteria on contact and preventing bacterial adhesion because of persistent bactericide diffusion, widespread application, no side effects, and a long lifetime [22–24].

The most common nanomaterials are graphene (Gr) and its derivatives, such as graphene oxide (GO) [25–27]. The potential of the antimicrobial attributes of GO versus different microorganisms, such as gram-positive and gram-negative bacterial pathogens, phytopathogens, and biofilm-forming microorganisms, has been reported in several papers [28–30]. The direct contact of sheets with bacterial cells causes physical and chemical interactions that mediate the antimicrobial activity of GO [31–34]. The first target of GO cytotoxicity in this process is the cell membrane, which can be damaged by the atomically sharp edges of Gr, leading to the physical disruption of coherence in the membrane by penetrating it [21,35–37]. Another benefit of GO sheets is its high antibacterial activity and biocompatibility in low concentration because of the large specific surface area and high fraction of surface atoms [26,38–39]. To the best of our knowledge, this is the first time that Mg-based nanocomposite containing GO has been fabricated and characterized to show its antibacterial and anticorrosive activities.

2. Experimental

First, pure Mg powder (99.8% purity, 50 μm average particle size), 3wt% Zn powder (98.8% purity, 7.5 μm average particle size), Mn powder (99.9% purity, 6.5 μm average particle size), and 0.5wt%–1.5wt% GO with 5–8 nm thickness and 750 m^2/g surface area, all of which were purchased from Sigma-Aldrich Co., USA, were mixed. In the present study, Mg matrix composites reinforced with GO were fabricated by the semi-powder metallurgy method. In this regard, the ultrasonication process was used by utilizing a 20 kHz ultrasonic cleaner machine (Alex Ultrasonic Cleaner 600 W). Then, to break the Van der Waals bond between carbon atoms, which could lead to the prevention of the aggregation of Gr particles, Gr was ultrasonicated in ethanol for 1 h. Next, Mg powder was added to the solution gradually. The mixture of GO and Mg powder was ultrasonicated for a quarter of an hour. Afterward, the mixture was stirred by a mechanical agitator at 2000 r/min for 2 h in a vacuum system. To remove ethanol from the mixture, the vacuum distillation system was utilized. Moreover, the mixture was dried at 400°C in a kiln with a controlled atmosphere under argon gas for approximately 3 h. Subsequently, dried Mg–Zn–Mn (MZM)/xGO powder was obtained through the complete removal of ethanol from the mixture. The obtained powder was ground at ambient temperature for 20 h under argon atmosphere using a controlled planetary ball mill. To prevent the generation of ample heat during ball milling, ethanol as a coolant was incorporated in the cups. The charge was loaded into a steel vial with a purified argon (<3 ppm oxygen) atmosphere. The controlled planetary ball mill was made of stainless steel balls with diameters of 10 and 20 mm for milling, where the ball-to-powder weight ratio was 20:1 (Fig. 1). For the compression test samples (ϕ10 mm × 15 mm) and other test samples (ϕ10 mm × 10 mm), the milled powders were compacted with the pressure of 400 MPa. Afterward, the specimens were sintered at 580°C for 2 h in a furnace under argon atmosphere. The parameters of the mechanical alloying process adopted for milling the MZM/xGO powders are presented in Table 1. Using Eq. (1) and on the basis of the volume percentages of Mg, Zn, and Mn, the theoretical density of the nanocomposites can be obtained.

$$\rho_{\text{composite}} = f_{\text{Mg}}\rho_{\text{Mg}} + f_{\text{Zn}}\rho_{\text{Zn}} + f_{\text{Mn}}\rho_{\text{Mn}} \tag{1}$$

where f and ρ are the volume fraction and theoretical density of each element, respectively. To verify the obtained bulk density, the following equation is used: Bulk density $= \frac{W_\text{d}}{W_\text{w} - W_\text{s}}$, where W_d is weigh of the dry sample, W_s and W_w are weighs of the dry samples when they are suspended in water and after they are removed from the water, respectively. The total porosity comprising a linked pore network can also be calculated using this equation. The cylindrical green compact of nanocomposites with a diameter of 10 mm and a height of 15 mm was pressed using the Instron 5569 universal testing machine (USA) at a crosshead speed of 0.5 mm/min and a load cell of 10 kN at room temperature to measure the compressive strength. Immersion tests of the specimens were conducted following the ASTM G31-72 standard. A Vickers hardness tester (LECO M-400, USA) with a force of 300 g (2.942 N) was employed to determine the microhardness values of the composite. Afterward, the specimens were washed with distilled water, ultrasonically degreased with ethanol, and dried at ambient temperature. On the basis of the scanning open-circuit potential (OCP), which was 1 mV/s, the voltage amplitude for the polarization tests was set between −0.25 and +0.25 V. The reference electrode was saturated calomel electrode (SCE), the counter electrode was the graphite (Gt) electrode, and the working electrode was the sample surface, which was linked to the electrolyte solution. Electrochemical impedance spectroscopy (EIS) tests were conducted following the ASTM G106 standard at a frequency range of 10^5 to 10^{-2} Hz under open-circuit conditions. The reproducibility of the results was evaluated by repeating every test three times. Table 2 presents the chemical composition of 200 mL of the Kokubo simulated body fluid (SBF) placed in a beaker, into which the samples were immersed according to Bakhsheshi-Rad *et al.* [19]. The pH value of the solution was adjusted to 7.6–7.7 at 37°C with 1.0 mol/L HCl and Tris. The beaker with SBF (with a pH value of 7.66) was sealed and incubated for 1 week at a fixed temperature of 37°C. Next, the samples

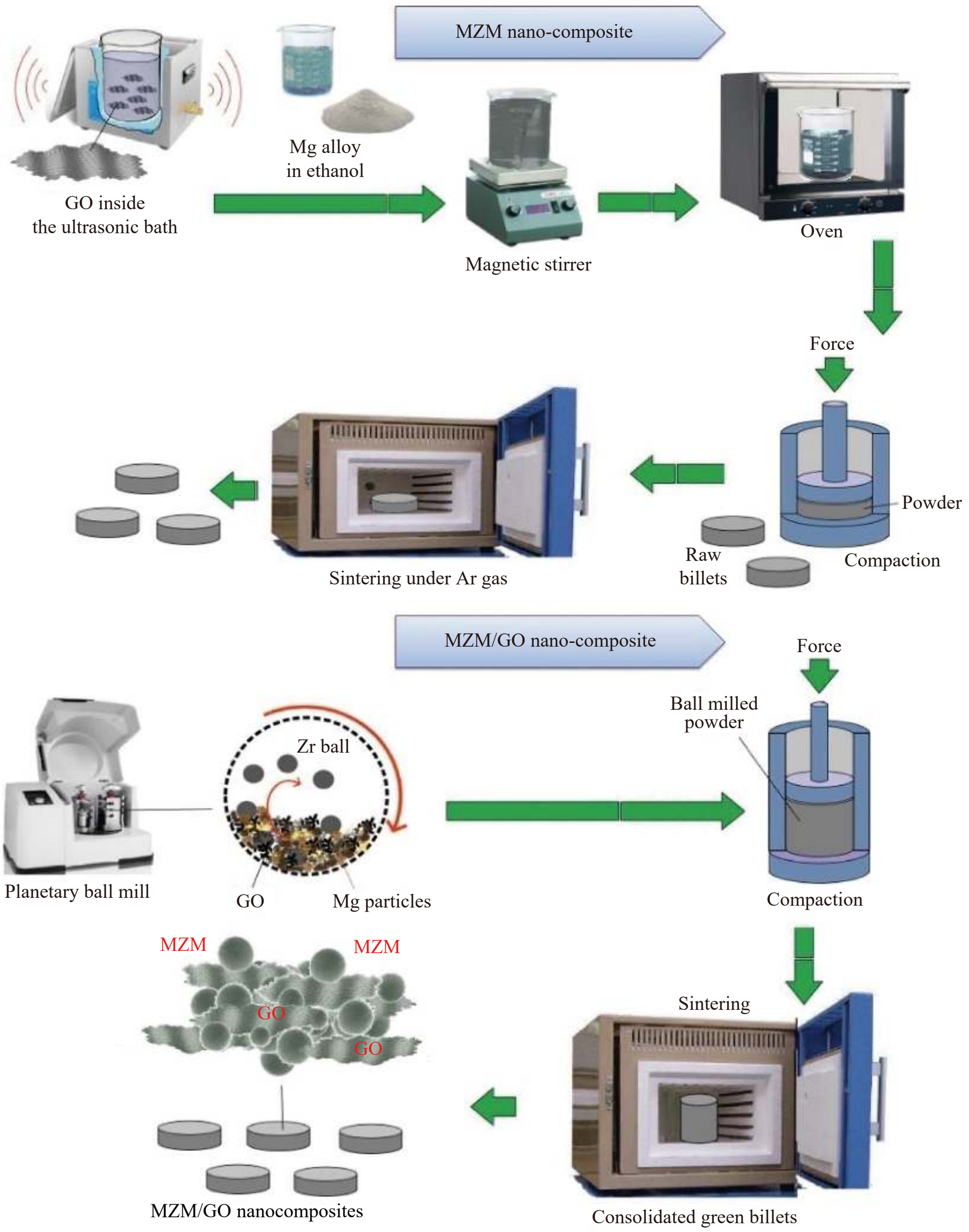

Fig. 1. Schematic diagram of the fabrication process for preparing MZM/GO nanocomposites.

Table 1. Parameters of the mechanical alloying process adopted for milling the powders

Rotation speed / ($r \cdot min^{-1}$)	250
Ball-to-powder weight ratio	20:1
Vial and ball material	Steel
Mass of powder / g	30
Milling time / h	20
Capacity of the vial / mL	250
Diameters of the balls / mm	10 and 20

were washed with acetone and deionized water, and the sample weight was measured after removing the corrosion products. The corrosion rate can be obtained using the following equation:

Table 2. Chemical composition of the Kokubo simulated body fluid (SBF) compared with the human blood plasma $mmol \cdot L^{-1}$

Solution	Na^+	K^+	Ca^{2+}	Mg^{2+}	HCO_3^-	Cl^-	HPO_4^{2-}	SO_4^{2-}
Human blood plasma	142.0	5.0	2.5	1.5	27.0	103.0	1.0	0.5
Kokubo SBF	142.0	5.0	2.5	1.5	4.2	147.8	1.0	0.5

$$C_R = \frac{W}{At\rho_{composite}} \tag{2}$$

where C_R is the corrosion rate, W is the mass loss, A is the surface area exposed to the corrosive media, t is the exposure time, and $\rho_{composite}$ is the density of composite. During the immersion test and after the 12 h time interval, the mean value of the pH of SBF from three measurements was recorded. Using scanning electron microscopy (SEM) and energy-dispersive spectroscopy (EDS), the surfaces of corroded specimens were analyzed.

To analyze the antibacterial behavior, disk diffusion, antibiotic sensitivity, and liquid medium microdilution requirements of nanocomposites, Salmonella–Shigella and Klebsiella pneumoniae bacteria were used. The inhibition zone (IZ) was used to analyze the antibacterial effect of nanocomposites containing different amounts of GO. To obtain the absorbance values of 0.1–0.2 at 625 nm, the Salmonella–Shigella and Klebsiella pneumoniae cultures were diluted with broth medium for one night. When the bacterial cultures were finished, the samples with the weight of 10 mg were added to the suspension and incubated at a temperature of 37°C. Afterward, the samples were shaken at a speed of 100 r/min on a platform shaker. To determine the absorbance value, a UV–Vis spectrophotometer (Lambda 25, USA) was utilized. Accordingly, using Eq. (3), bacterial inhibition was calculated by recording the absorbance value of every examined solution at 625 nm at 4 and 24 h time intervals. In this equation, I_C is the bacterial suspension absorbance value and I_S is the bacterial value of every suspension comprising one of the three different nanocomposites including GO.

$$\text{Bacterial inhibition (\%)} = \frac{I_C - I_S}{I_C} \times 100 \tag{3}$$

In the extraction method, an indirect 3-(4,5-dimethylthiazol-2-yl)-2,5-diphenyltetrazolium bromide (MTT; Sigma-Aldrich, St. Louis, MO, USA) assay was used to determine the *in vitro* cytotoxicity of nanocomposites containing different amounts of GO. By injecting 100 µL of dimethyl sulfoxide (DMSO) into the wall, the formazan crystals were dissolved after 4 h. Then, an ELISA Reader (Stat Fax 2100 Microplate Reader; Awareness Technology, Miami, FL, USA) was used to read the absorbance at 545 nm, and a cell-free culture medium was utilized as a control group to normalize the nanocomposites according to Lonardelli *et al.* [14]. To analyze the effect of tetracycline on the early osteogenic differentiation of MG63 cells, on the third and seventh days, the alkaline phosphatase (ALP) activity assay was conducted. The cells were seeded at a concentration of 104 cells/mL placed individually in a 24-well plate. According to Lonardelli *et al.* [14], the cells were left to grow in a damp atmosphere of 5% CO_2/95% air at 37°C for several days. To investigate the microstructure of the Mg-based nanocomposite, SEM (JEOL JSM-6380LA, JEOL Ltd., Tokyo Japan) and transmission electron microscopy (TEM; HT7700, Hitachi Ltd., Tokyo, Japan) were used. The phase components were identified using an X-ray diffractometer (Siemens D5000, Germany) with Cu K_α radiation (45 kV, 40 mA) over the diffraction angles (2θ) of 20° to 80° at a scanning speed of 4°/min. Finally, the Williamson–Hall equation was used to determine the crystallite size of the nanocomposite [30].

3. Results and discussion

3.1. Morphological characterization

The field emission scanning electron microscope (FESEM) micrographs of the MZM nanocomposite are shown in Fig. 2(a)–(d). The distributions of Zn and Mn in Mg

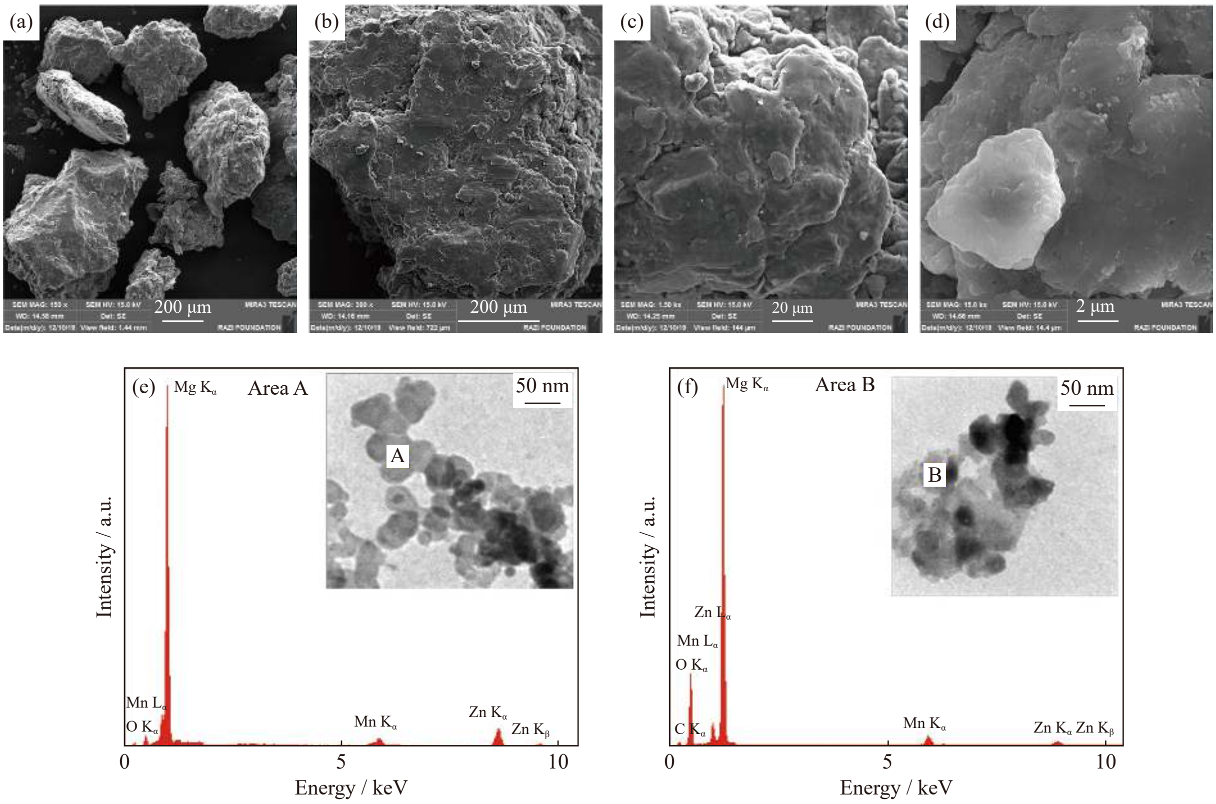

Fig. 2. FESEM micrographs of (a–d) MZM nanocomposites with different magnifications and energy dispersive spectroscopy (EDS) analyses of (e) area A and (f) area B. The insets in (e) and (f) show the corresponding TEM images of the MZM nanoparticles.

were uniform because the primary powder particle sizes of Mg, Mn, and Zn did not vary. The small particle size of Mg led to high surface reactivity; thus, it was difficult to utilize. Meanwhile, the amounts of Mn and Zn in the structure were only 1wt% and 3wt%, respectively, due to preventing inherited risk concentration of Zn and Mn in localized regions of the composite structure. To achieve a uniform dispersion of these particles, it is better to have small particle sizes of Zn and Mn along with a large specific surface area. Uniform and fine distributions of Zn and Mn powders were observed in the Mg matrix along with their monotonous adhesion to the surface of Mg powder. As shown in Fig. 2(e) and (f), Zn and Mn are always present on the surface of Mg, which is verified by the elemental analysis (i.e., EDS) of the surface of MZM mixed powder.

Fig. 3 shows the SEM morphology of the MZM/*x*GO nanocomposite powders, indicating that some aggregates are formed by GO nanosheets. Notably, GO uniformly distributed in the MZM/*x*GO nanocomposites matrix which could have significant effect on the mechanical and corrosion property of the composite as shown in Fig. S1 in Supplementary Information. Moreover, the GO nanosheets loaded on MZM nanocomposite and placed within the matrix of the MZM nanocomposite (Fig. 3(b)–(d)). The EDS spectrum confirms the presence of Mg, Mn, Zn, C, and O, which further confirms the presence of GO in the MZM matrix (i.e., areas A and B). The presence of C peaks can be attributed to GO embedded in the Mg-based nanocomposite structure. In this context, the FESEM micrographs and related EDS analysis of sintered MZM/GO nanocomposites with different amounts of GO are presented in Fig. S2 in Supplementary Information.

Fig. 4 shows the EDS mapping of Mg, Zn, and Mn in MZM nanocomposites with and without GO. The continuous shape of the particles, including Mg, Zn, and Mn, is also shown in the EDS mapping. In the case of the incorporation of GO in the nanocomposite, the existence of GO in the MZM/GO nanocomposite was verified by the existence of the element C. In this context, when pre-dispersion was done, individual GO was embedded on the MZM particle surface. Ideal dispersion of GO occurs at this stage because of incomplete reduction, in which GO is transformed from graphite oxide and slightly functionalized with the carboxyl group (–COOH) at the edges [22]. Notably, in comparison with the MZM matrix, this phenomenon is expected because of the discrepancy between the density of the MZM matrix and the density of GO, with the increase in GO resulting in the low reduction of the densities. GO has a less significant influence on the level of composite porosity because the range of porosity is approximately 4% to 5% under the same compaction pressure.

Fig. 5 shows the TEM images of the MZM/*x*GO nanocomposites. The GO nanosheets are denoted by dark lines (Fig. 5(a) and (b)), while the MZM nanoparticles are denoted by bold dark spheres and gray regions. The GO plate presen-

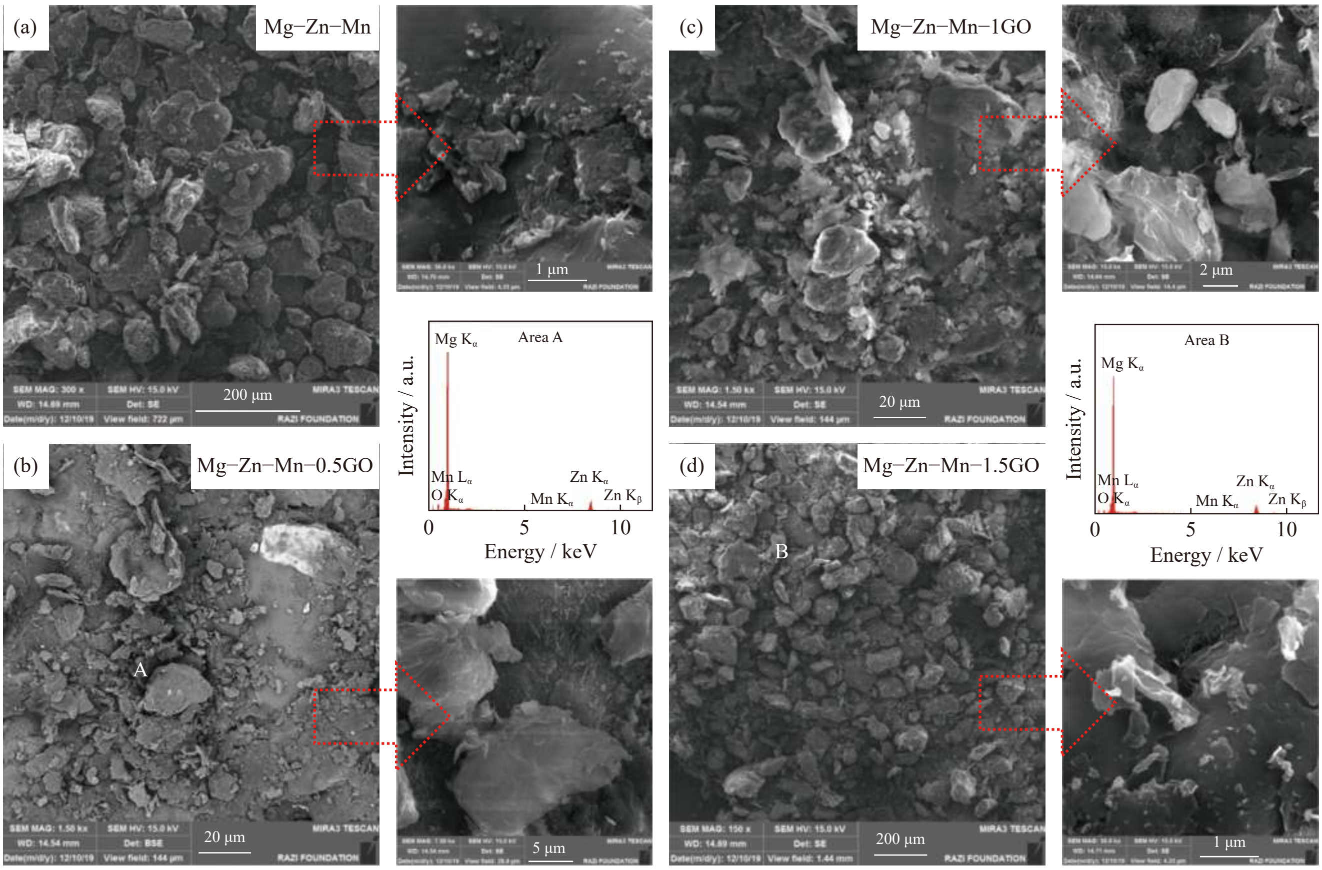

Fig. 3. FESEM micrographs of (a) MZM, (b) MZM/0.5GO, (c) MZM/1GO, and (d) MZM/1.5GO nanocomposites, and EDS analyses of area A in (b) and area B in (d).

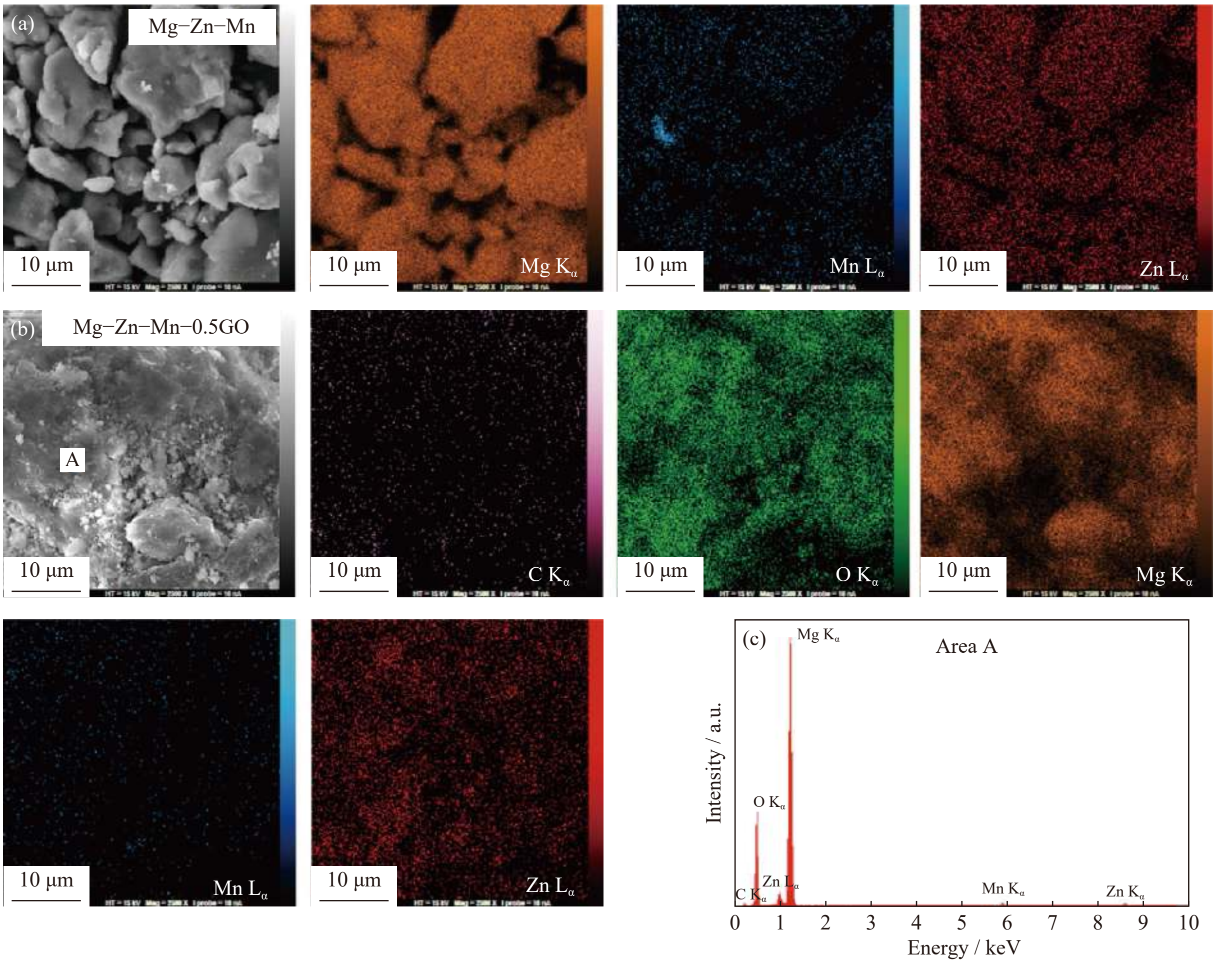

Fig. 4. FESEM micrographs and corresponding element maps of the (a) MZM nanocomposite and (b) MZM/0.5GO nanocomposite; (c) EDS analysis of area A in (b).

ted as exfoliated sheets exhibited uniform dispersion in the Mg-based matrix without agglomeration. Moreover, the size of the MZM nanoparticles that formed on the surface of GO sheets was less than 100 nm. Furthermore, the MZM nanoparticles exhibited monotonous propagation on the surface of GO nanosheets without accumulation, as shown in the TEM images (Fig. 5(c)–(e)). The EDS spectrum from Area A confirms the presence of Mg, Mn, Zn, C, and O, which further confirms the presence of GO in the MZM matrix.

The X-ray diffractometer (XRD) patterns of the GO and MZM/*x*GO nanocomposite samples are shown in Fig. 5(f). The XRD patterns of the MZM alloy, GO, and MZM/GO nanocomposite samples indicated that the MZM alloy includes α-Mg with a hexagonal close-packed crystalline structure and $Mg_{12}Zn_{13}$ phase. The crystallite size of the nanocomposites calculated using the Williamson–Hall equation was approximately 19–46 nm, which was validated by the TEM images. However, GO exhibited a major diffraction peak at 9.8° with a lattice spacing of 0.9 nm [14,21]. For the MZM/GO nanocomposite, the diffraction peaks identified at 32.1°, 34.3°, 36.4°, 47.3°, 57.2°, 62.8°, 68.1°, 69.8°, 77.8°, and 81.2° were related to α-Mg [18], not GO. GO was possibly not detected by the XRD instrument because of its low amount [40] or the loss of normal and periodic arrangement of GO nanosheets due to the fine exfoliation and dispersion of GO in the matrix. The Fourier transform-infrared (FTIR) spectra of GO (Fig. 5(g)) showed two bands at 1334 and 1590 cm^{-1}, which were related to the D and G bands [40–41], respectively. The disorder and faults in carbon atoms cause the D band, and the sp^2 in-plane vibration of carbon atoms causes the G band [41]. The existence of GO was proven by the D and G bands identified in the GO nanosheet and Mg-based nanocomposite containing GO. Moreover, the positions of the D and G bands in the GO nanosheet/Mg-based nanocomposite containing GO changed from 1590 to 1595 cm^{-1} and from 1334 to 1329 cm^{-1}, respectively [21,40]. The hydrogen bonding interaction between the oxygen-containing functional groups of GO and the oxygen-containing functional groups of a thin layer of MgO that formed on the surface of Mg could cause a solid interaction between GO and the MZM matrix, which could be the reason for the aforementioned change in position. The spectrum of the observable peaks in the range of 3444 to 3641 cm^{-1} is related to the stretching vibration of the O–H bonds. A peak related to the stretching vibration of the O–H bond is also observed at 1642 cm^{-1} [21].

Fig. 6 shows the wettability of the MZM/GO nanocomposite analyzed through water contact angle (WCA) measurement. The WCA of the MZM nanocomposite was 62.3°, which was slightly more than the boundary of hydrophobi-

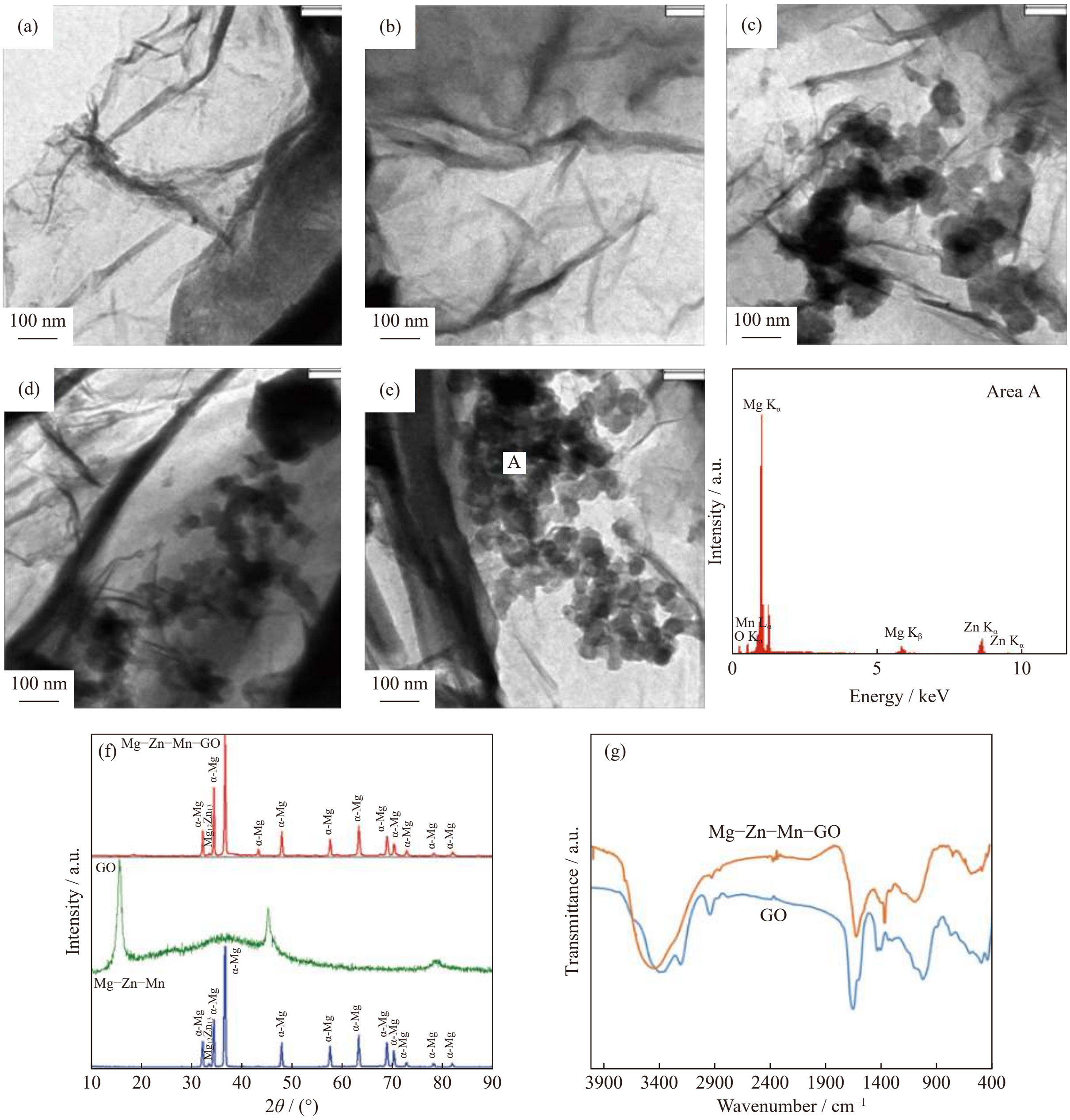

Fig. 5. TEM images of (a, b) GO, (c) MZM/0.5GO, (d) MZM/1GO, and (e) MZM/1.5GO nanocomposites and the corresponding EDS analysis of area A. (f) XRD patterns of the MZM nanocomposite, GO, and MZM/1GO nanocomposite, and (g) FTIR spectra of GO and MZM/1GO nanocomposite.

city. The WCA of the nanocomposite containing 0.5wt% GO was less than 57.4°, indicating the change in its characteristics from hydrophobic to hydrophilic. The WCA of the MZM/1GO nanocomposite (i.e., 55.8°) was slightly less than that of the MZM nanocomposite; however, the MZM/1.5GO nanocomposite showed a much lower WCA (47.1°). The WCA of GO was 23.7°, indicating the hydrophilic nature of GO, which was the reason for the increase in the wettability of the nanocomposite.

3.2. Antibacterial properties

Using the paper disk diffusion method, the antibacterial activity of the MZM/*x*GO nanocomposites was analyzed versus Salmonella–Shigella and Klebsiella pneumoniae bacteria. Fig. 7(a)–(d) show the inhibition zones (IZ) of the MZM/*x*GO nanocomposites and the numerical values of the diameter of IZ. As shown in the figure, the MZM/1.5GO nanocomposites exhibited a more significant toxic effect on bacteria than the MZM/0.5GO nanocomposite under identical conditions. Moreover, the amount of GO in the matrix and the type of utilized bacteria significantly influenced the antibacterial activity of the prepared beads. The MZM/1.5GO nanocomposite exhibited higher antibacterial activity than the MZM/0.5GO and MZM/1GO nanocomposites. Similarly, the diameters of the IZ of the MZM/0.5GO, MZM/1GO, and MZM/1.5GO nanocomposites were 1.91, 3.32, and 3.61 mm, respectively, against Salmonella–Shigella bacteria. The presence of GO sheets in the MZM matrix could be the reason for the antibacterial activity of the MZM/GO nanocomposite. In this regard, Hegab *et al.* [24] first documented the antibac-

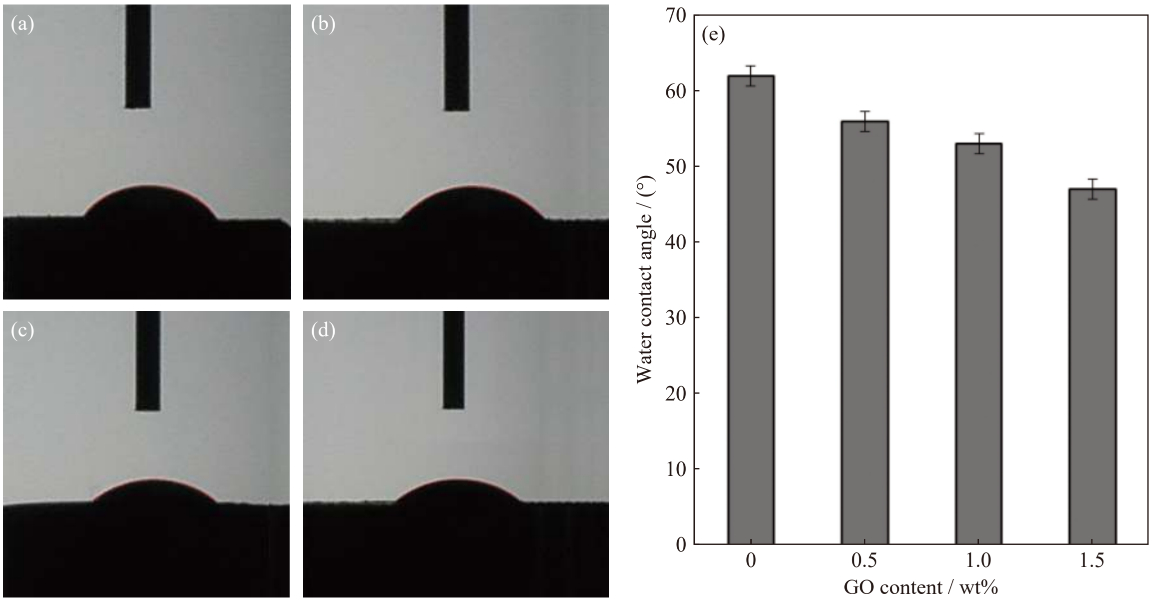

Fig. 6. Images of the contact angles of (a) MZM, (b) MZM/0.5GO, (c) MZM/1GO, and (d) MZM/1.5GO nanocomposites, and (e) values of the contact angles of the MZM/*x*GO nanocomposites.

terial activity of Gt in 2016, where Gr was observed to significantly damage and cause the dysfunction of the bacteria attached to it. Notably, the cell membrane was damaged, showing that the proposed composite had an efficient and rapid effect on Escherichia coli and Staphylococcus aureus. The results of the tests showed that Gr nanosheets exhibited higher antibacterial activity than typical antibiotics, such as kanamycin. GO, like Gr, showed good antibacterial performance toward several bacteria because GO is an oxidized Gr sheet with innumerous oxygen-containing functional groups. The comparison between GO, Gt, Gr, and reduced GO showed that GO exhibited the highest bactericidal activity against Escherichia coli [21,24,40]. Cell damage is due to oxidative stress caused by the existence of nanocomposites. According to Hegab *et al.* [24], the inhibitory property of nanocomposites containing Gr was enhanced.

Fig. 7(e) presents the possible synergistic antibacterial mechanism of the MZM/GO nanocomposite. Notably, the number of Salmonella–Shigella bacteria was significantly reduced on the MZM/GO nanocomposite. Moreover, their cellular structures were considerably damaged. When their cell membrane components are separated and disintegrated, Salmonella–Shigella bacteria become distorted and shrunken. The antibacterial activity of MZM nanocomposite containing GO leads to powerful antibacterial features. GO, which is an unparalleled sheet-like nanomaterial, could interact with the cell membrane components of bacteria, such as lipids and proteins, via hydrogen bonding, electrostatic, π–π stacking, and Van der Waals interactions because it has several special specifications, including a large amount of oxygen-containing functional groups on the surface, a large π-conjugated structure, a large specific surface area, and a negative charge [21,24,33]. GO nanosheets can adsorb onto bacterial cells and cover them via this interaction. The bacterial cytomembrane can be physically damaged by the infiltration of the sharp edges of GO nanosheets. Hence, the antibacterial performance of the nanocomposite embedded with GO is significantly increased [24].

3.3. Cytocompatibility

Fig. 8(a) shows the MTT assay results of MG63 cells cultured on the nanocomposites for 3 and 7 d. The number of live cells is relative to the absorbance. Notably, the increase in culture time slowly increases the numbers of live cells on the MZM/GO nanocomposite containing 0.5wt% and 1wt% GO, indicating that cell proliferation increases with increasing GO content. By contrast, the number of live cells on the MZM/GO nanocomposite with a high GO content is lower than that on the composite containing low amount of GO after 3 and 7 d of culture, indicating the negative effect of high GO content on cell proliferation. This behavior further confirms that excess amounts of GO considerably affect cell proliferation. The oxygen-containing functional groups of GO on the surface could be the reason for its stimulatory effects. According to Zhang *et al.* [42], the hydroxyl groups of GO could enhance cell adhesion by providing sites for maintaining and recruiting cells onto the nanocomposite. According to Guo *et al.* [43], cell growth could be increased by GO, which provided a platform for the creation of a biointerface. Liu *et al.* [21] reported that cell adhesion and proliferation could be promoted by the hydrophilic groups of GO. According to Gao *et al.* [38], the hydroxyl groups of GO could secure sites to retain and recruit cells onto the scaffold, resulting in the improvement of cell adhesion. Moreover, Shuai *et al.* [36], Munir *et al.* [37], and Gao *et al.* [38] reported that a platform for the creation of a biointerface for cell growth was provided by graphene nanoplatelets (GNPs). According to Munir *et al.* [37], the encapsulation of GNPs in pure Mg and Mg-based matrix did not have any adverse effect on cell response. ALP activity was considered a quantitative marker of osteogenesis. In this investigation, the cell response of the MZM/GO nanocomposite to MG63 cells and its influence on

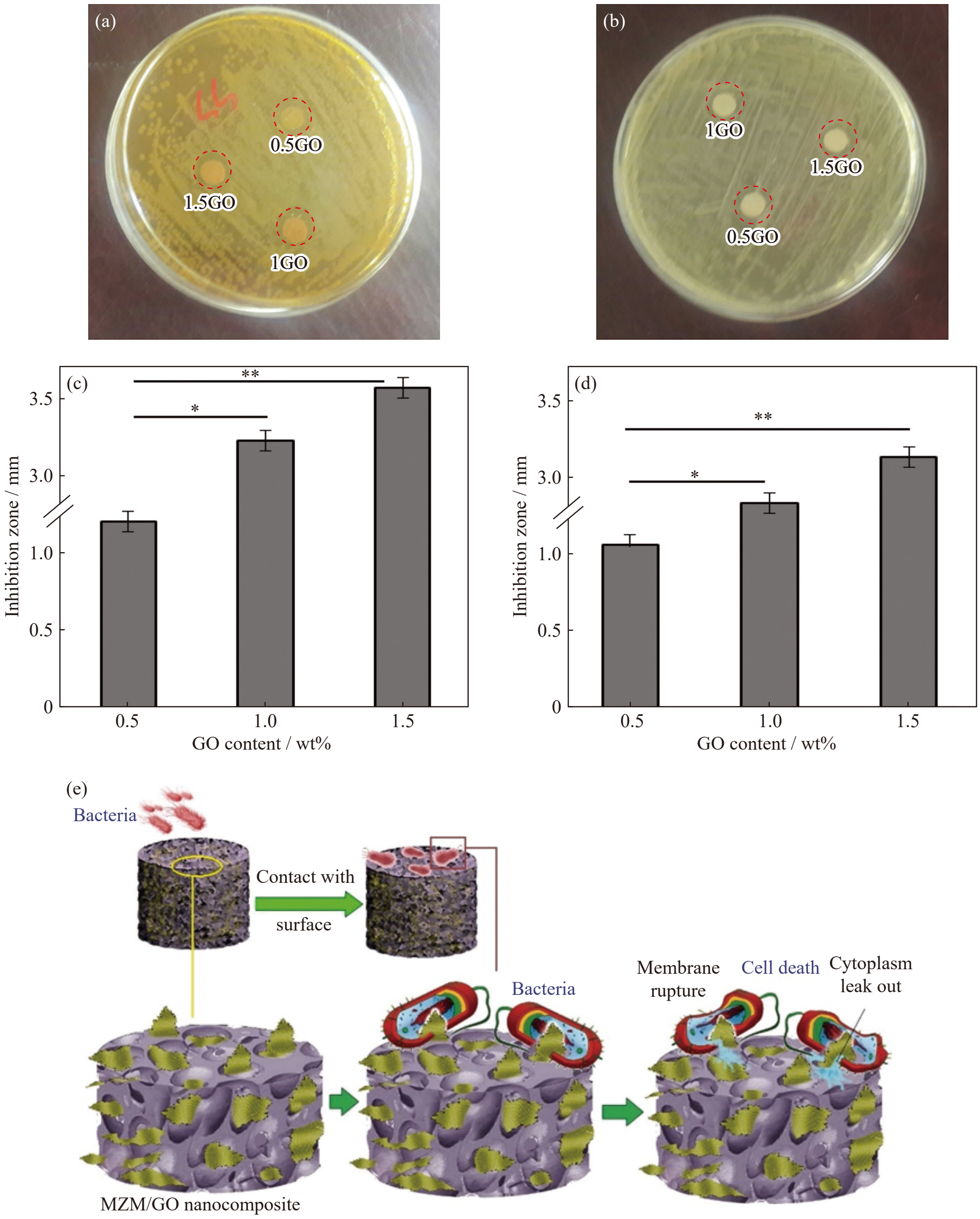

Fig. 7. Antibacterial activities of the MZM/*x*GO nanocomposites against (a) Salmonella–Shigella and (b) Klebsiella pneumoniae analyzed using the disk diffusion test. Diameters of the inhibition zones for the MZM/*x*GO nanocomposites against (c) Salmonella–Shigella and (d) Klebsiella pneumonia. The statistical significance is indicated by probability (*p*) as follows: **p*-value < 0.05; ***p*-value < 0.01. (e) Schematic diagram of the antimicrobial mechanism of the MZM/*x*GO nanocomposites against Salmonella–Shigella bacteria.

osteogenesis were assessed using the ALP activity assay (Fig. 8(b)). No considerable alteration in the ALP activity can be observed for the MZM/GO nanocomposite with a low GO content compared with the MZM alloy. By contrast, the ALP activity of the MZM/GO nanocomposite with a high GO content was reduced, which also showed that excess amounts of GO have a negative effect on osteogenesis.

3.4. Corrosion behavior

Fig. 8(c) presents the potentiodynamic polarization curves of the samples immersed in the SBF solution. The OCPs were determined after immersion for 15 min, and the applied potential was between −250 and +250 mV (at a scanning rate of 5 mV/s). The corrosion potential (E_{corr}) values of the nanocomposites reinforced with GO transferred to the anodic area, showing that the corrosion performance of the reinforced composites was decreased. Notably, the MZM/0.5GO (−1435.46 mV vs. SCE) and MZM/1GO (−1469.82 mV vs. SCE) nanocomposites shifted to a more noble potential than the MZM nanocomposite (−1519.12 mV vs. SCE), as shown in Table 3. However, the figure does not show the relationship between corrosion performance and GO content of the

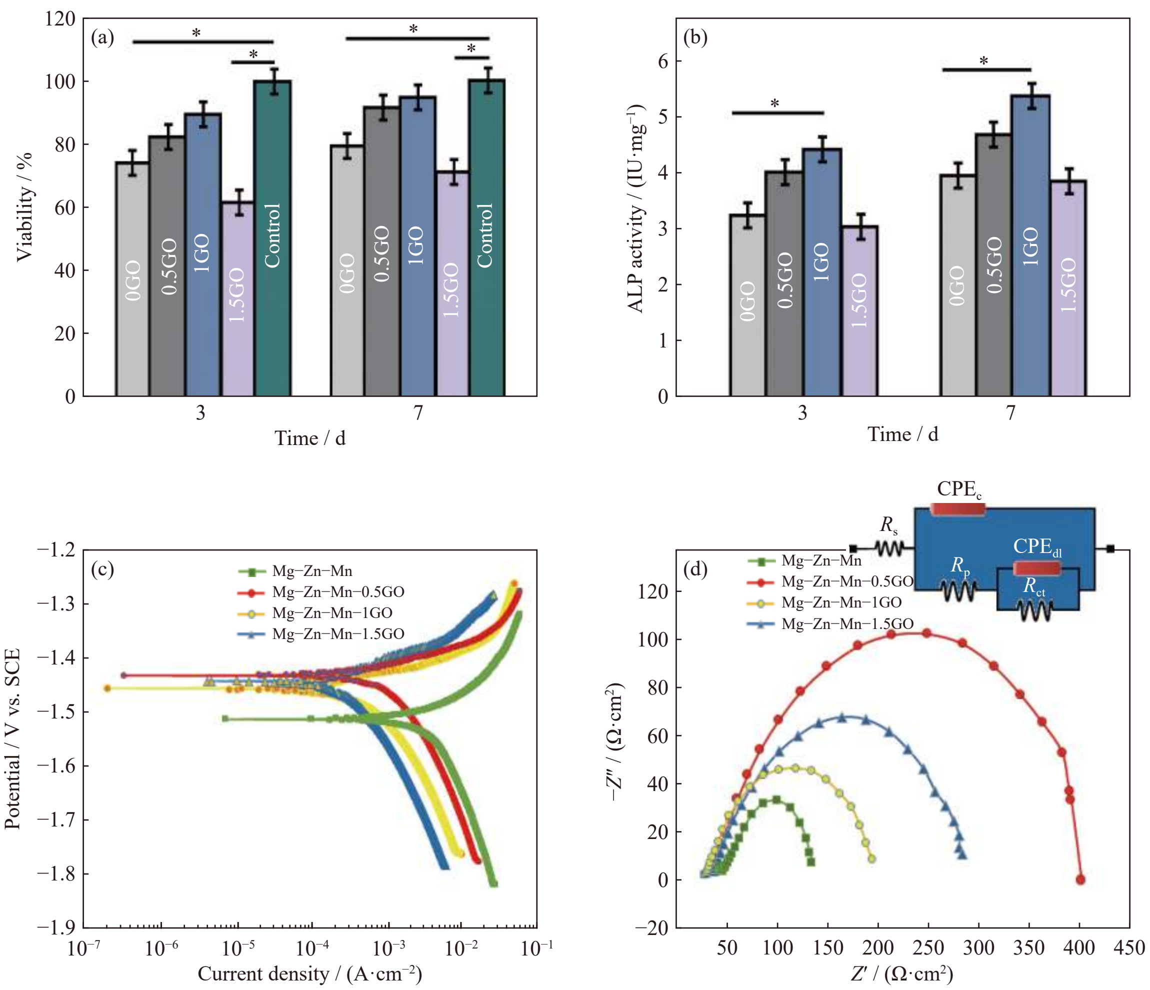

Fig. 8. (a) Cell viability and (b) ALP activity of MG63 cells cultured for different times on the nanocomposites (*$p < 0.05$). (c) Potentiodynamic polarization curves and (d) Nyquist plots and corresponding equivalent circuit of a constant time employed for the MZM/*x*GO nanocomposites.

Table 3. Electrochemical parameters of the specimens immersed in the Kokubo SBF during the polarization tests

Sample	E_{corr} / mV vs. SCE	i_{corr} / (μA·cm^{-2})	C_R / (mm·a^{-1})
MZM	−1519.12	338.41	7.73
MZM/0.5GO	−1435.46	127.52	2.91
MZM/1GO	−1469.82	175.78	4.01
MZM/1.5GO	−1442.11	245.27	5.60

reinforced sample because of the diverse potentiodynamic behavior in the cathodic and anodic parts of nanocomposites with different amounts of GO [42–45]. Thus, the corrosion current density (i_{corr}) that could be applied via Tafel extrapolation to the corrosion data needs to be calculated accurately. The corrosion rates (C_R) of the samples can be calculated using the i_{corr} values obtained from extrapolations using the following equation [19]:

$$C_R = i_{corr} \times 22.85 \tag{4}$$

Remarkably, the MZM/0.5GO (127.52 μA·cm^{-2}) and MZM/1GO (175.78 μA·cm^{-2}) nanocomposites exhibited a lower current density than the MZM (338.41 μA·cm^{-2}) nanocomposite. This trend indicated that corrosion performance could be increased by a low content (0.5wt%) of GO, although i_{corr} could be significantly increased with the addition of GO with high content. The excess GO accelerates corrosion because it serves as an effective cathode; therefore, a large amount of GO in the MZM/GO nanocomposites enhances the corrosion rate. However, the overall corrosion performance could be decreased by excess amount of GO, compared to the MZM nanocomposite. Consequently, a micro-galvanic reaction occurs between Mg and GO. These results are consistent with the results obtained for CNT-reinforced Mg composite in a previous study [46].

EIS tests of the MZM/GO nanocomposites immersed in the SBF solution were conducted to further confirm the results of the polarization tests. The EIS tests (Fig. 8(d)) show that the value of corrosion resistance is normally obtained from the value of charge transfer resistance (R_{ct}). A high R_{ct} value (large arc) enhances the anticorrosion performance. Moreover, the higher the R_{ct} value, the higher the corrosion resistance of the prepared nanocomposite. The samples were characterized by a simple equivalent expression, where R_s is the solution resistance, CPE$_c$ is capacitance of corrosion products layer, R_p is resistance relating to micropore or ionic conducting defect resistance, and CPE$_{dl}$ is the double-layer capacitance parallel to the charge transfer resistance at the interface between the electrolyte and the Mg-based composite (the high frequency capacitance loop). The fitting results show that the MZM nanocomposite without GO ((142.5 ± 34) $\Omega\cdot cm^2$) has lower R_{ct} value than MZM/0.5GO nanocomposite ((422.3 ± 44) $\Omega\cdot cm^2$), MZM/1GO ((288.4 ± 15) $\Omega\cdot cm^2$), and MZM/1.5GO ((197.6 ± 19) $\Omega\cdot cm^2$) nanocomposites. These results are consistent with the results of the polarization tests. The high corrosion resistance of MZM/0.5GO nanocomposites is due to the existence of a small amount of GO, which prevents ion transport (Cl^- ion) to the MZM matrix. GO embedded in the MZM matrix hinders the penetration of SBF into the MZM matrix, hence enhancing the corrosion resistance of the MZM matrix.

The corrosion mechanism can be understood by analyzing the surfaces of corroded specimens up to 7 d. As shown in Fig. 9(a)–(h), Mg-based nanocomposites with a small amount of GO have uniform corrosion surfaces. However, with the addition of GO, pitting formations are observed. The grain boundaries start the corrosion process, and the increase in immersion time enhances the corrosion rate. Consequently, the addition of reinforcements reduces the corrosion behavior of the samples. Galvanic corrosion possibly occurs between the additive (i.e., GO) and the MZM matrix. Therefore, in the long term, the matrix starts to dissolve, and the reinforcements detach from the nanocomposite. As shown in Fig. 9(i), the EDS spectra indicate that the precipitate layer on the composite surface consists of Ca, P, Mg, C, and O, which signify the creation of hydroxyapatite (HAp) during immersion. The Ca/P molar ratio of neat MZM alloy is approximately 1.32. However, the MZM/1GO nanocomposite maintained the Ca/P molar ratio at 1.41, which is nearly similar to the value of natural bone (i.e., 1.67). The oxygen-containing functional groups of GO [36] could be the cause of the high Ca/P molar ratio of MZM/GO, which decrease the corrosion rate, increase the deposition of apatite on the MZM/1GO nanocomposite, and protect the α-Mg matrix from the invasion of body fluids moderately.

The pH values of the MZM and MZM/GO nanocomposite specimens immersed in the SBF solution after 7 d are presented in Fig. 9(j). The effortless corrosion of the samples immersed in the SBF solution can be observed, which can be attributed to the rapid increment of the pH values of the MZM/GO nanocomposite with a large amount of GO at the starting point and the highest possible pH value of (10.63 ± 0.23). However, a small change in the pH value of MZM/0.5GO and MZM/1GO nanocomposites was observed, i.e., approximately (8.34 ± 0.15) and (8.61 ± 0.17), respectively. Hence, the anticorrosion performance of MZM with a low amount of GO was increased because of the slow chemical dissolution [38].

Weight loss was measured for the analyzed MZM/GO nanocomposites after 7 d, as shown in Fig. 9(k). Remarkably, MZM with a small amount of GO, i.e., MZM/0.5GO and MZM/1GO nanocomposites, exhibited nearly identical performance. By contrast, the increase in immersion time intervals leads to the reduction of the corrosion resistance of the MZM/GO nanocomposite with a large amount of GO. This study shows the long-term corrosion performance of MZM nanocomposites reinforced with GO. According to the literature [36], GO can bridge the cracks in the corrosion layer and hinder it from falling off the surface of the matrix; thus, this thin layer acts as a barrier layer that prevents further penetration of SBF, thereby increasing the corrosion resistance.

The schematic diagram of the degradation process and apatite formation mechanism of the MZM/GO nanocomposite specimens immersed in the SBF solution is shown in Fig. 9(l). The electrochemical corrosion resistance and the formation of pits are reduced by the penetration of SBF solution ions into the MZM/GO nanocomposite during the primary immersion time interval once the MZM/GO nanocomposite is immersed in the SBF solution. Concurrently, Mg^{2+} and H_2 gases are generated by the alkaline media surrounding the Mg-based matrix because of the dissolution of the MZM/GO nanocomposite [36]. Moreover, the oxygen-containing functional groups of GO nanosheets can promote the deposition of apatite on the Mg matrix because the penetration of SBF is prevented by the compact apatite film, which is a beneficial site provided by the GO nanosheets for HAp nucleation [6,36]. Notably, the interaction between the GO nanosheets as reinforcements and the corrosion products could hinder their detachment from the matrix. However, eventually, the corrosion products would be eliminated, and the penetration of SBF into the Mg alloy matrix would occur. Subsequently, the degradation process of the MZM/GO nanocomposite would occur.

3.5. Mechanical properties

As shown in Fig. 10(a), by conducting compressive tests and using the indentation method, the mechanical properties of the nanocomposite specimens were determined. Notably, the increment of the GO content up to 1wt% enhanced the compressive strength. The addition of GO from 0wt% to 1wt% leads to the increase in the fracture toughness of the sintered specimens, indicating that the incorporation of GO improves the fracture toughness of the MZM nanocomposite. However, the mechanical performance decreased because the excess increase (1.5wt%) in GO content could be related to the aggregation of GO. Thus, the addition of 0.5wt%–1wt% of GO can enhance the mechanical properties of the MZM nanocomposites to a considerable extent. Grain refinement and stress transfer from the Mg matrix to GO enhanced the mechanical properties. The common toughening mechanisms of Gr-based materials include the following: (a) crack bridging, where crack diffusion is delayed by the GO sheets by connecting the two surfaces of the crack and providing closure stress to counter the applied stress; (b) pullout mechanism, where the matrix is pulled out by Gr, causing the interfacial friction between GO sheets and the matrix, which consequently reduces crack diffusion; (c) crack deflection, where after encountering the GO sheets, the crack is diverted to another surface, resulting in a twisted path, which leads to considerable energy loss [26,30,37–38]; (d) crack tip shielding, where the crack tip is limited near the GO sheets be-

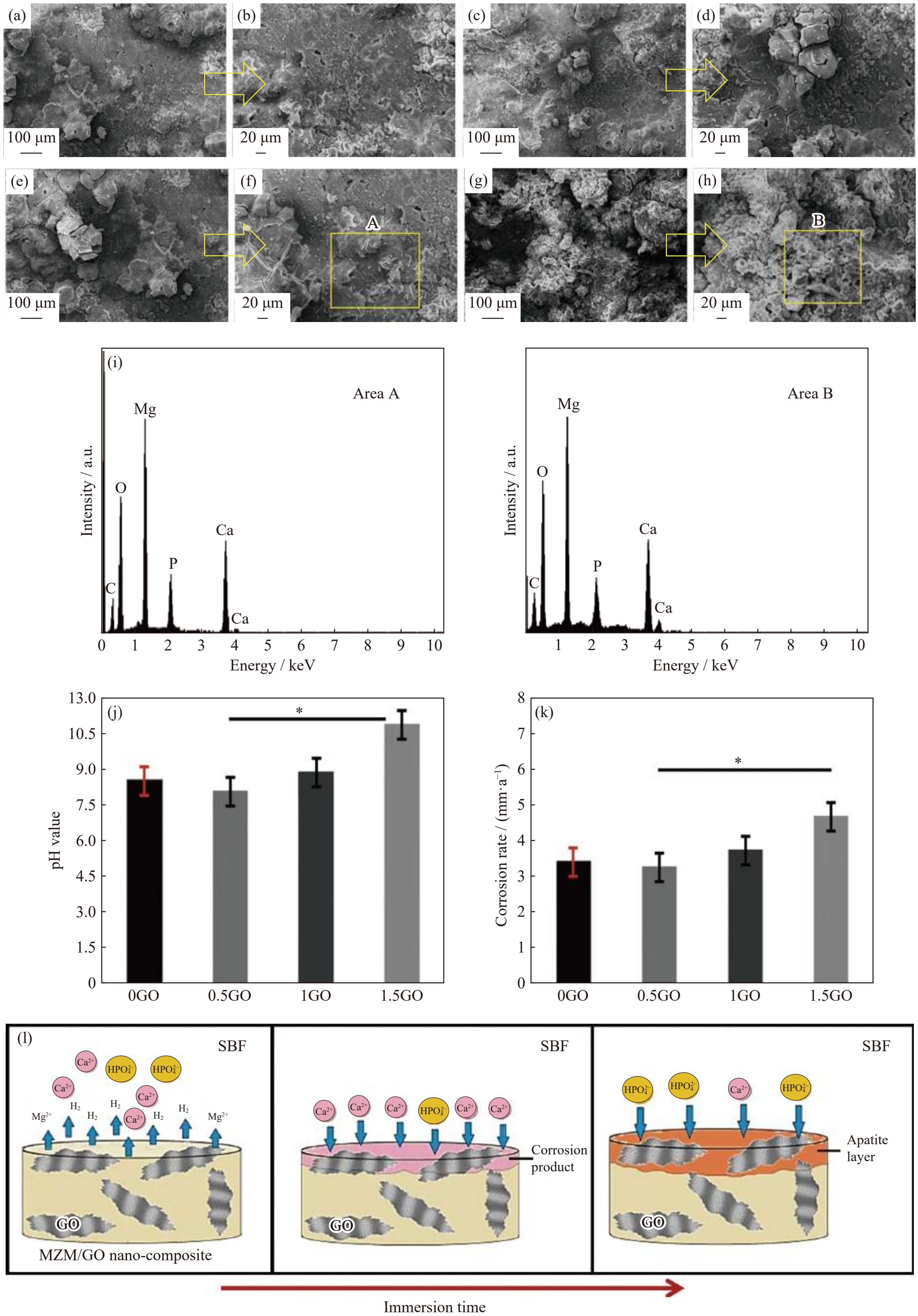

Fig. 9. Corrosion surfaces of the (a, b) MZM, (c, d) MZM/0.5GO (e, f) MZM/1GO, and (g, h) MZM/1.5GO nanocomposites after immersion for 7 d. (i) EDS analyses of area A in (f) and area B in (h). (j) pH values and (k) weight loss measurements of the MZM/*x*GO nanocomposites (*$p < 0.05$). (l) Schematic diagram of apatite formation and deposition on the surface of the MZM/GO nanocomposite.

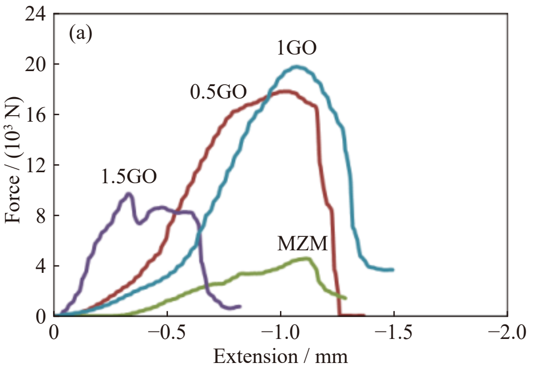

(b)

Material	Micro hardness, HV	Compression strength / N	Extension / mm
MZM composite	49	4820	1.12
MZM/0.5GO	59	17810	1.31
MZM/1GO	63	19960	1.44
MZM/1.5GO	64	9620	0.72

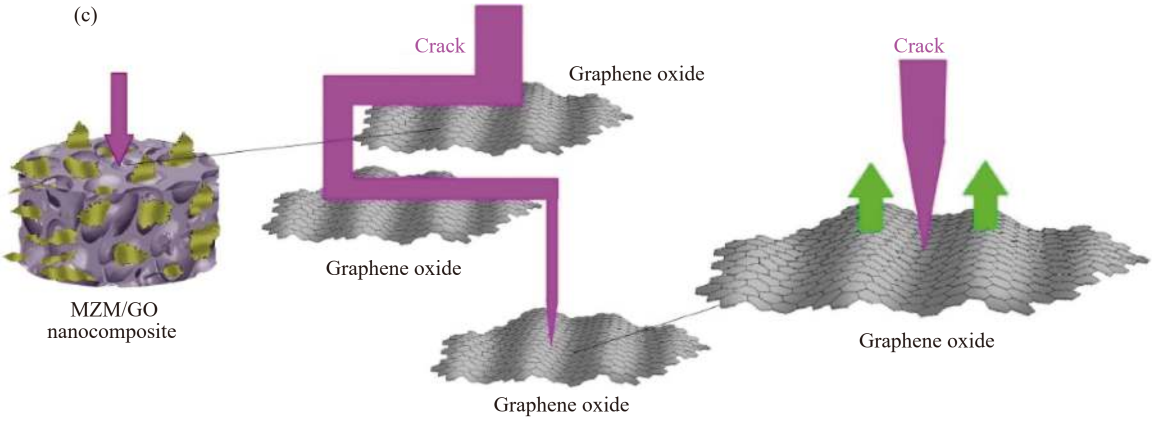

Fig. 10. (a) Typical compressive curves and (b) hardness and compressive strength values of the MZM/*x*GO nanocomposites; (c) schematic diagram of the crack deflection toughening mechanisms of GO in the MZM/*x*GO nanocomposites.

cause of inadequate strength to break the interface bonding [37].

Fig. 10(b) presents the average hardness results of the composites after measuring the hardness of every specimen three times. Large amounts of GO reinforcements considerably enhance the hardness and mechanical performance because the GO reinforcements serve as an obstacle to dislocation motion. Moreover, the Vickers hardness increases because of the Van der Waals bond between carbon atoms and interface bonding between the matrix and the reinforcements. The dislocation density increases because of inhomogeneous deformation caused by the existence of hard and high elastic modulus reinforcements [22,37–38]. The MZM/1.5GO nanocomposite exhibits the highest hardness value among the synthesized composites because of the large specific surface area of the GO reinforcements. A uniform distribution is observed in the matrix because of the weak Van der Waals bond between carbon atoms, which can considerably affect the mechanical properties [38–39].

Fig. 10(c) shows the schematic diagram of the enhancement mechanisms related to the toughening mechanisms. When a matrix crack is started and spread, because of the variations in the elastic modulus, the load shifts from the matrix to the GO sheets. The effective mechanical interconnection and load transition in the Mg-based matrix are due to the wrinkled surface texture of GO sheets. In this regard, crack bridging, a toughening mechanism where the GO sheet bridges two crack surfaces, is observed. The stress needed for crack diffusion is reduced by GO, which disrupts the relative displacement between the opposing crack surfaces. As shown in the figure, once the shear stress at the interface becomes more than the interfacial strength of Mg-based nanocomposite with GO sheet, pullout of the GO sheets starts. Because the GO sheet has a high hardness value and a large specific surface area, this process wastes more energy. Resistance from the interfacial friction between the GO sheet and the Mg matrix can considerably reduce crack propagation. The crack deflection toughening mechanism is shown in the figure [44–46]. First, a crack spreads in the Mg-based matrix, and once it encounters GO, the crack diverts to another plane. As the crack plane is not perpendicular to the axis of stress anymore, the crack needs more energy to diffuse. Furthermore, the deflection process causes more energy loss because it produces an indirect path for crack diffusion [38,47–52]. Crack deflection could be beneficial for GO-based materials because of the large specific surface area. Because of inadequate energy to break the interface bonding, the crack tip is limited near GO. The mechanical improvement gets saturated with GO amounts of 0.5wt%–1wt%, as the excess GO (2wt%) is tough to disperse uniformly in the Mg-based matrix.

4. Conclusion

In this study, using the semi-powder metallurgy method, different contents of GO were embedded in the Mg–Zn–Mn (MZM) matrix to prepare MZM/*x*GO nanocomposites for orthopedic applications. The corrosion performance and the mechanical and biological characteristics of the MZM/*x*GO nanocomposites were analyzed. The microstructural assessment showed that a uniform distribution was achieved in the MZM/0.5GO and MZM/1GO nanocomposite specimens. However, agglomeration was observed in the MZM/1.5GO nanocomposite specimen. The results showed that the GO content, hardness value, and compressive strength are positively associated. In this context, the MZM/1GO nanocomposite has higher hardness value and compressive strength than the Mg-based nanocomposite without GO. The MZM/0.5GO nanocomposite exhibited a nearly comparable corrosion resistance to the MZM/1GO nanocomposite, even though the incorporation of more GO has an unfavorable effect on the R_{ct} value of the MZM matrix. The MTT assay results showed that the MZM/1GO nanocomposite increased the MG63 cell viability and ALP activity, indicating the increasing level of osteogenesis. The results of the analysis of antibacterial activity showed that the MZM/1.5GO nanocomposite had a noticeable effect on antibacterial effectiveness toward bacteria, including Salmonella–Shigella and Klebsiella pneumoniae. In summary, the results indicate the possibility of utilizing the MZM/1GO nanocomposite for implant applications with effective anti-infection characteristics.

Conflict of Interest

The authors declare that they have no competing/financial conflict of interest in this paper.

Supplementary Information

The online version contains supplementary material available at https://doi.org/10.1007/s12613-020-2201-2

Additional file 1: **Fig. S1.** FESEM micrographs of (a) MZM/0.5GO, (b) MZM/1GO and (c) MZM/1.5GO nano-composites. **Fig. S2.** FESEM micrographs of as-sintered composites: (a) MZM, (b) MZM/0.5GO, (c) MZM/1GO, and (d) MZM/1.5GO nano-composites; EDS analyses of (e) area A in (c) and (f) area B in (d).

References

[1] A.H.M. Sanchez, B.J.C. Luthringer, F. Feyerabend, and R. Willumeit, Mg and Mg alloys: How comparable are *in vitro* and *in vivo* corrosion rates? A review, *Acta Biomater.*, 13(2015), p. 16.

[2] P. Xiong, Z.J. Jia, M. Li, W.H. Zhou, J.L. Yan, Y.H. Wu, Y. Cheng, and Y.F. Zheng, Biomimetic Ca, Sr/P-doped silk fibroin films on Mg–1Ca alloy with dramatic corrosion resistance and osteogenic activities, *ACS Biomater. Sci. Eng.*, 4(2018), No. 9, p. 3163.

[3] N. Li and Y.F. Zheng, Novel magnesium alloys developed for biomedical application: A review, *J. Mater. Sci. Technol.*, 29(2013), No. 6, p. 489.

[4] Y.J. Chen, Z.G. Xu, C. Smith, and J. Sankar, Recent advances on the development of magnesium alloys for biodegradable implants, *Acta Biomater.*, 10(2014), No. 11, p. 4561.

[5] H.R. Bakhsheshi-Rad, E. Hamzah, S.L.J. Yii, A. Mostafa, R. Ebrahimi-Kahrizsangi, and M. Medraj, Characterisation and thermodynamic calculations of biodegradable Mg–2.2Zn–3.7Ce and Mg–Ca–2.2Zn–3.7Ce alloys, *Mater. Sci. Technol.*, 33(2017), No. 11, p. 1333.

[6] M. Ali, M.A. Hussein, and N. Al-Aqeeli, Magnesium-based composites and alloys for medical applications: A review of mechanical and corrosion properties, *J. Alloys Compd.*, 792(2019), p. 1162.

[7] Y.F. Zheng, X.N. Gu, and F. Witte, Biodegradable metals, *Mater. Sci. Eng. R*, 77(2014), p. 1.

[8] A.V. Koltygin, V.E. Bazhenov, R.S. Khasenova, A.A. Komissarov, A.I. Bazlov, and V.A. Bautin, Effects of small additions of Zn on the microstructure, mechanical properties and corrosion resistance of WE43B Mg alloys, *Int. J. Miner. Metall. Mater.*, 26(2019), No. 7, p. 858.

[9] H.R. Bakhsheshi-Rad, E. Hamzah, A.F. Ismail, M. Aziz, M. Daroonparvar, S. Parham, Z. Hadisi, and M.A.M. Yajid, Titania–carbon nanotubes nanocomposite coating on Mg alloy: Microstructural characterisation and mechanical properties, *Mater. Sci. Technol.*, 34(2018), No. 4, p. 378.

[10] M.S. Song, R.C. Zeng, Y.F. Ding, R.W. Li, M. Easton, I. Cole, N. Birbilis, and X.B. Chen, Recent advances in biodegradation controls over Mg alloys for bone fracture management: A review, *J. Mater. Sci. Technol.*, 35(2019), No. 4, p. 535.

[11] D.Q. Wan, Y.L. Hu, S.T. Ye, Z.M. Li, L.L. Li, and Y. Huang, Effect of alloying elements on magnesium alloy damping capacities at room temperature, *Int. J. Miner. Metall. Mater.*, 26(2019), No. 6, p. 760.

[12] Y.F. Zheng, X.N. Gu, Y.L. Xi, and D.L. Chai, *In vitro* degradation and cytotoxicity of Mg/Ca composites produced by powder metallurgy, *Acta Biomater.*, 6(2010), No. 5, p. 1783.

[13] I. Lonardelli, M. Bortolotti, W. van Beek, L. Girardini, M. Zadra, and H.K.D.H. Bhadeshia, Powder metallurgical nanostructured medium carbon bainitic steel: Kinetics, structure, and *in situ* thermal stability studies, *Mater. Sci. Eng. A*, 555(2012), p. 139.

[14] I. Lonardelli, L. Girardini, L. Maines, C. Menapace, A. Molinari, and H.K.D.H. Bhadeshia, Nanostructured bainitic steel obtained by powder metallurgy approach: Structure, transformation kinetics and mechanical properties, *Powder Metall.*, 55(2012), No. 4, p. 256.

[15] F. Witte, The history of biodegradable magnesium implants: A review, *Acta Biomater.*, 6(2010), No. 5, p. 1680.

[16] Y.Z. Ma, C.L. Yang, Y.J. Liu, F.S. Yuan, S.S. Liang, H.X. Li, and J.S. Zhang, Microstructure, mechanical, and corrosion properties of extruded low-alloyed Mg–*x*Zn–0.2Ca alloys, *Int. J. Miner. Metall. Mater.*, 26(2019), No. 10, p. 1274.

[17] Y.Y. Song, H.K.D.H. Bhadeshia, and D.W. Suh, Stability of stainless-steel nanoparticle and water mixtures, *Powder Technol.*, 272(2015), p. 34.

[18] M. Razzaghi, M. Kasiri-Asgarani, H.R. Bakhsheshi-Rad, and H. Ghayour, Microstructure, mechanical properties, and *in-vitro* biocompatibility of nano-NiTi reinforced Mg–3Zn–0.5Ag alloy: Prepared by mechanical alloying for implant applications, *Composites Part B*, 190(2020), art. No. 107947.

[19] H.R. Bakhsheshi-Rad, M.R. Abdul-Kadir, M.H. Idris, and S. Farahany, Relationship between the corrosion behavior and the thermal characteristics and microstructure of Mg–0.5Ca–*x*Zn alloys, *Corros. Sci.*, 64(2012), p. 184.

[20] M. Khosravi, M. Mansouri, A. Gholami, and Y. Yaghoubinezhad, Effect of graphene oxide and reduced graphene oxide nanosheets on the microstructure and mechanical properties of mild steel jointing by flux-cored arc welding, *Int. J. Miner. Metall. Mater.*, 27(2020), No. 4, p. 505.

[21] C. Liu, J. Shen, K.W.K. Yeung, and S.C. Tjong, Development and antibacterial performance of novel polylactic acid–graphene oxide–silver nanoparticle hybrid nanocomposite mats prepared by electrospinning, *ACS Biomater. Sci. Eng.*, 3(2017), No. 3, p. 471.

[22] Ö. Güler and N. Bağcı, A short review on mechanical properties of graphene reinforced metal matrix composites, *J. Mater. Res. Technol.*, 9(2020), No. 3, p. 6808.

[23] S. Ramezanzade, G.R. Ebrahimi, M.T. Parizi, and H.R. Ezatpour, Microstructure and mechanical characterizations of graphene nanoplatelets-reinforced Mg–Sr–Ca alloy as a novel composite in structural and biomedical applications, *J. Compos. Mater.*, 54(2020), No. 5, p. 711.

[24] H.M. Hegab, A. ElMekawy, L. Zou, D. Mulcahy, C.P. Saint, and M. Ginic-Markovic, The controversial antibacterial activity of graphene-based materials, *Carbon*, 105(2016), p. 362.

[25] Q.H. Yuan, G.H. Zhou, L. Liao, Y. Liu, and L. Luo, Interfacial structure in AZ91 alloy composites reinforced by graphene nanosheets, *Carbon*, 127(2018), p. 177.

[26] M. Rashad, F.S. Pan, M. Asif, and A. Ullah, Improved mechanical properties of magnesium–graphene composites with copper–graphene hybrids, *Mater. Sci. Technol.*, 31(2015), No. 12, p. 1452.

[27] J.L. Su, J. Teng, Z.L. Xu, and Y. Li, Biodegradable magnesium-matrix composites: A review, *Int. J. Miner. Metall. Mater.*, 27(2020), No. 6, p. 724.

[28] X. Du, W.B. Du, Z.H. Wang, K. Liu, and S.B. Li, Ultra-high strengthening efficiency of graphene nanoplatelets reinforced magnesium matrix composites, *Mater. Sci. Eng. A*, 711(2018), p. 633.

[29] M. Wang, Y. Zhao, L.D. Wang, Y.P. Zhu, X.J. Wang, J. Sheng, Z.Y. Yang, H.L. Shi, Z.D. Shi, and W.D. Fei, Achieving high strength and ductility in graphene/magnesium composite via an *in situ* reaction wetting process, *Carbon*, 139(2018), p. 954.

[30] V.B. Mohan, K.T. Lau, D. Hui, and D. Bhattacharyya, Graphene-based materials and their composites: A review on production, applications and product limitations, *Composites Part B*, 142(2018), p. 200.

[31] M. Pul, Effect of sintering temperature on pore ratio and mechanical properties of composite structure in nano graphene reinforced ZA27 based composites, *Int. J. Miner. Metall. Mater.*, 27(2020), No. 2, p. 232.

[32] M. Rashad, F.S. Pan, H.H. Hu, M. Asif, S. Hussain, and J. She, Enhanced tensile properties of magnesium composites reinforced with graphene nanoplatelets, *Mater. Sci. Eng. A*, 630(2015), p. 36.

[33] W. Han, Z.N. Wu, Y. Li, and Y.Y. Wang, Graphene family nanomaterials (GFNs)—Promising materials for antimicrobial coating and film: A review, *Chem. Eng. J.*, 358(2019), p. 1022.

[34] W.M. Tian, S.M. Li, B. Wang, X. Chen, J.H. Liu, and M. Yu, Graphene-reinforced aluminum matrix composites prepared by spark plasma sintering, *Int. J. Miner. Metall. Mater.*, 23(2016), No. 6, p. 723.

[35] L.Q. Wu, R.Z. Wu, L.G. Hou, J.H. Zhang, and M.L. Zhang, Microstructure, mechanical properties and wear performance of AZ31 matrix composites reinforced by graphene nanoplatelets (GNPs), *J. Alloys Compd.*, 750(2018), p. 530.

[36] C.J. Shuai, B. Wang, Y.W. Yang, S.P. Peng, and C.D. Gao, 3D honeycomb nanostructure-encapsulated magnesium alloys with superior corrosion resistance and mechanical properties, *Composites Part B*, 162(2019), p. 611.

[37] K.S. Munir, C.E. Wen, and Y.C. Li, Carbon nanotubes and graphene as nanoreinforcements in metallic biomaterials: A review, *Adv. Biosyst.*, 3(2019), No. 3, art. No. 1800212.

[38] C.D. Gao, P. Feng, S.P. Peng, and C.J. Shuai, Carbon nanotube, graphene and boron nitride nanotube reinforced bioactive ceramics for bone repair, *Acta Biomater.*, 61(2017), p. 1.

[39] F. Samadpour, G. Faraji, and A. Siahsarani, Processing of AM60 magnesium alloy by hydrostatic cyclic expansion extrusion at elevated temperature as a new severe plastic deformation method, *Int. J. Miner. Metall. Mater.*, 27(2020), No. 5, p. 669.

[40] C.J. Shuai, W. Guo, P. Wu, W.J. Yang, S. Hu, Y. Xia, and P. Feng, A graphene oxide–Ag co-dispersing nanosystem: Dual synergistic effects on antibacterial activities and mechanical properties of polymer scaffolds, *Chem. Eng. J.*, 347(2018), p. 322.

[41] X.F. Zou, L. Zhang, Z.J. Wang, and Y. Luo, Mechanisms of the antimicrobial activities of graphene materials, *J. Am. Chem. Soc.*, 138(2016), No. 7, p. 2064.

[42] B. Zhang, P. Wei, Z.X. Zhou, and T.T. Wei, Interactions of graphene with mammalian cells: Molecular mechanisms and biomedical insights, *Adv. Drug Delivery Rev.*, 105(2016), p. 145.

[43] C.X. Guo, X.T. Zheng, Z.S. Lu, X.W. Lou, and C.M. Li, Biointerface by cell growth on layered graphene–artificial peroxidase–protein nanostructure for *in situ* quantitative molecular detection, *Adv. Mater.*, 22(2010), No. 45, p. 5164.

[44] O. Guler, Y. Say, and B. Dikici, The effect of graphene nanosheet (GNS) weight percentage on mechanical and corrosion properties of AZ61 and AZ91 based magnesium matrix composites, *J. Compos. Mater.*, 54(2020), No. 28, p. 4473.

[45] M.E. Turan, Y. Sun, F. Aydin, H. Zengin, Y. Turen, and H. Ahlatci, Effects of carbonaceous reinforcements on microstructure and corrosion properties of magnesium matrix composites, *Mater. Chem. Phys.*, 218(2018), p. 182.

[46] Y. Say, O. Guler, and B. Dikici, Carbon nanotube (CNT) reinforced magnesium matrix composites: The effect of CNT ratio on their mechanical properties and corrosion resistance, *Mater. Sci. Eng. A*, 798(2020), art. No. 139636.

[47] Y. Mei, P.Z. Shao, M. Sun, G.Q. Chen, M. Hussain, F.L. Huang, Q. Zhang, X.S. Gao, Y.Y. Pei, S.J. Zhong, and G.H. Wu, Deformation treatment and microstructure of graphene-reinforced metal matrix nanocomposites: A review of graphene post-dispersion, *Int. J. Miner. Metall. Mater.*, 27(2020), No. 7, p. 888.

[48] X. Zeng, J. Teng, J.G. Yu, A.S. Tan, D.F. Fu, and H. Zhang, Fabrication of homogeneously dispersed graphene/Al composites by solution mixing and powder metallurgy, *Int. J. Miner. Metall. Mater.*, 25(2018), No. 1, p. 102.

[49] H.M. Xia, L. Zhang, Y.C. Zhu, N. Li, Y.Q. Sun, J.D. Zhang, and H.Z. Ma, Mechanical properties of graphene nanoplatelets reinforced 7075 aluminum alloy composite fabricated by spark plasma sintering, *Int. J. Miner. Metall. Mater.*, 27(2020), No. 9, p. 1295.

[50] P.H. Chen, Y. Zhang, R.Q. Li, Y.X. Liu, and S.S. Zeng, Influence of carbon-partitioning treatment on the microstructure, mechanical properties and wear resistance of *in situ* VCp-reinforced Fe-matrix composite, *Int. J. Miner. Metall. Mater.*, 27(2020), No. 1, p. 100.

[51] H. Pal and V. Sharma, Mechanical, electrical, and thermal expansion properties of carbon nanotube-based silver and silver–palladium alloy composites, *Int. J. Miner. Metall. Mater.*, 21(2014), No. 11, p. 1132.

[52] Z.C. Hou, L.Q. Xiong, Y.F. Liu, L. Zhu, and W.Z. Li, Preparation of super-aligned carbon nanotube-reinforced nickel-matrix laminar composites with excellent mechanical properties, *Int. J. Miner. Metall. Mater.*, 26(2019), No. 1, p. 133.